Complex THz and DC inverse spin Hall effect in YIG/Cu$_{1-x}$Ir$_x$ bilayers across a wide concentration range

Joel Cramer,[†,‡] Tom Seifert,[¶] Alexander Kronenberg,[†] Felix Fuhrmann,[†] Gerhard Jakob,[†,‡] Martin Jourdan,[†] Tobias Kampfrath,[¶,§] and Mathias Kläui[∗,†,‡]

†*Institute of Physics, Johannes Gutenberg-University Mainz, 55099 Mainz, Germany*
‡*Graduate School of Excellence Materials Science in Mainz, 55128 Mainz, Germany*
¶*Department of Physical Chemistry, Fritz Haber Institute of the Max Planck Society, 14195 Berlin, Germany*
§*Department of Physics, Freie Universität Berlin, 14195 Berlin, Germany*

E-mail: Klaeui@uni-mainz.de
Fax: 0049-6131-39-24076

Abstract

We measure the inverse spin Hall effect of Cu$_{1-x}$Ir$_x$ thin films on yttrium iron garnet over a wide range of Ir concentrations ($0.05 \leqslant x \leqslant 0.7$). Spin currents are triggered through the spin Seebeck effect, either by a DC temperature gradient or by ultrafast optical heating of the metal layer. The spin Hall current is detected by, respectively, electrical contacts or measurement of the emitted terahertz radiation. With both approaches, we reveal the same Ir concentration dependence that follows a novel complex, non-monotonous behavior as compared to previous studies. For small Ir concentrations a signal minimum is observed, while a pronounced maximum appears near the equiatomic composition. We identify this behavior as originating from the interplay of different spin Hall mechanisms as well as a concentration-dependent variation of the integrated spin current density in Cu$_{1-x}$Ir$_x$. The coinciding results obtained for DC and ultrafast stimuli provide further support that the spin Seebeck effect extends to terahertz frequencies, thus enabling a transfer of established spintronic measurement schemes into the terahertz regime. Our findings also show that the studied material allows for efficient spin-to-charge conversion even on ultrafast timescales.

Keywords

Spin Hall Effect, Spin Seebeck Effect, Ultrafast spin currents, Alloy

Spin currents are a promising ingredient for the implementation of next-generation, energy-efficient spintronic applications. Instead of exploiting the electronic charge, transfer as well as processing of information is mediated by spin angular momentum. Crucial steps towards the realization of spintronic devices are the efficient generation, manipulation and detection of spin currents at highest speeds possible. Here, the spin Hall effect (SHE) and its inverse (ISHE) are in the focus of current research[1] as they allow for an interconversion of spin and charge currents in heavy metals with strong spin-orbit interaction (SOI). The efficiency of this conversion is quantified by the spin Hall angle θ_{SH}.

In general, the SHE has intrinsic as well as extrinsic spin-dependent contributions. The intrinsic SHE results from a momentum-space Berry phase effect and can, amongst others,

1

be observed in $4d$ and $5d$ transition metals[1–3]. The extrinsic SHE, on the other hand, is a consequence of skew and side-jump scattering off impurities or defects[4]. It occurs in (dilute) alloys of normal metals with strong SOI impurity scatterers[5–8], but can also be prominent in pure metals in the superclean regime[9]. As a consequence, the type of employed metals and the alloy composition are handles to adjust and maximize the SHE. Remarkably, it was recently shown that the SHE in alloys of two heavy metals (e.g. AuPt) can even exceed the SHE observed for the single alloy partners[10]. Pioneering work within this research field covered the extrinsic SHE by skew scattering in copper-iridium alloys[5]. However, previously the iridium concentration was limited to $12\,\%$ effective doping of Cu with dilute Ir. The evolution of the SHE in the alloy regime for large concentration thus remains an open question and the achievable maximum by an optimized alloying strategy is unknown.

The potential of a metal for spin-to-charge conversion, i.e. θ_{SH}, can be determined by injecting a spin current and measuring the resulting charge response. This can be accomplished by, for instance, coherent spin pumping through ferromagnetic resonance[11–13] or the spin Seebeck effect (SSE)[14,15]. The SSE describes the generation of a magnon spin current along a temperature gradient within a magnetic material. Typically, such experiments involve a heterostructure composed of a magnetic insulator, such as yttrium iron garnet (YIG), and the ISHE metal under study [see Fig. 1(a)]. A DC temperature gradient in the YIG bulk is induced by heating the sample from one side. On the femtosecond time scale, in contrast, a temperature difference across the YIG-metal interface can be induced by heating the metal layer with an optical laser pulse [Fig. 1(b)][16–19]. We have recently shown that the resulting ultrafast spin current can be interpreted as an ultrafast version of the SSE[19].

For ultrafast laser excitation, the resulting sub-picosecond ISHE current leads to the emission of an electromagnetic pulse with a spectrum extending into the terahertz (THz) range, which can be detected by optical means[20].

Therefore, femtosecond laser excitation offers the remarkable benefit of contact-free measurements of the ISHE current without any need of micro-structuring the sample. The all-optical generation as well as detection of ultrafast electron spin currents[20,21] are key requirements for transferring spintronic concepts into the THz range[22]. So far, however, the SSE-type characterization of the ISHE was conducted by employing DC spin currents [Fig. 1(a)]. For the use in ultrafast applications and to further corroborate our notion of an ultrafast SSE, it remains to be shown whether alloying yields the same notable changes of the spin-to-charge conversion efficiency in ultrafast experiments [Fig. 1(b)] and whether alloys can provide an efficient spin-to-charge conversion even at THz frequencies.

In this Letter, we study the compositional dependence of the ISHE in YIG/$\mathrm{Cu}_{1-x}\mathrm{Ir}_x$ bilayers over a wide concentration range ($0.05 \leqslant x \leqslant 0.7$), exceeding the dilute doping phase investigated in previous studies[5]. The ISHE response of $\mathrm{Cu}_{1-x}\mathrm{Ir}_x$ is measured as a function of x, for which both the DC and ultrafast SSE are employed. Eventually, we compare the spin-to-charge conversion efficiency in the two highly distinct regimes of DC and terahertz dynamics across a wide alloying range.

The YIG samples used for this study are of $870\,\mathrm{nm}$ thickness, grown epitaxially on (111)-oriented $\mathrm{Gd}_3\mathrm{Ga}_5\mathrm{O}_{12}$ (GGG) substrates by liquid-phase-epitaxy. After cleaving the GGG/YIG into samples of dimension $2.5\,\mathrm{mm} \times 10\,\mathrm{mm} \times 0.5\,\mathrm{mm}$, $\mathrm{Cu}_{1-x}\mathrm{Ir}_x$ thin films (thickness $d_{\mathrm{CuIr}} = 4\,\mathrm{nm}$) of varying composition ($x = 0.05, 0.1, 0.2, 0.3, 0.5$ and 0.7) are deposited by multi-source magnetron sputtering from two elemental Cu and Ir targets. During the sputtering process, the argon gas pressure of $5 \times 10^{-3}\,\mathrm{mbar}$ and the sample temperature of $\approx 300\,\mathrm{K}$ are kept constant, whereas the rf powers applied to the targets are varied individually to adjust the alloy composition according to previously determined power-dependent growth rates. For more detailed information and film characterization via X-ray reflectometry, see the Supporting Information. To prevent oxidation of the metal film, a $3\,\mathrm{nm}$ Al capping layer
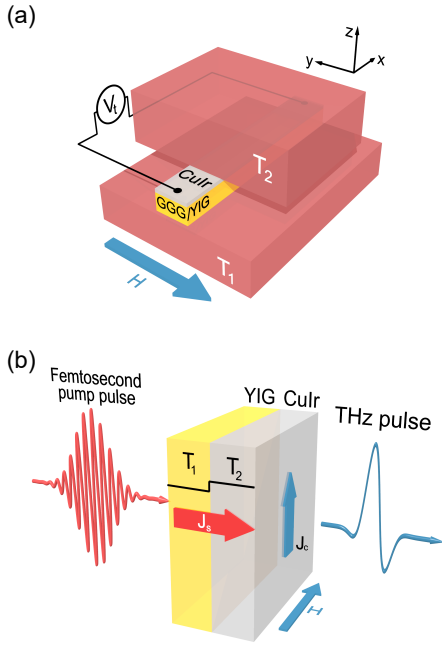
Figure 1: (a) Schematic of the setup used for DC SSE measurements. The out-of-plane temperature gradient is generated by two copper blocks set to individual temperatures T_1 and T_2. An external magnetic field is applied in the sample plane. The resulting thermovoltage V_t is recorded by a nanovoltmeter. (b) Schematic of the contact-free ultrafast SSE/ISHE THz emission approach. The in-plane magnetized sample is illuminated by a femtosecond laser pulse, inducing a step-like temperature gradient across the YIG/Cu$_{1-x}$Ir$_x$ interface. The SSE-induced THz spin current in the CuIr layer is subsequently converted into a sub-picosecond in-plane charge current by the ISHE, thereby leading to the emission of a THz electromagnetic pulse into the optical far-field.

is deposited, which, when exposed to air, forms an AlO$_x$ protection layer. For the contact-free ultrafast SSE measurements, patterning of the Cu$_{1-x}$Ir$_x$ films into defined nanostructures is unnecessary. In the case of DC SSE measurements, the film is contacted for the detection of the thermal voltage.

The DC SSE measurements are performed at room temperature in the conventional longitudinal configuration[15]. While an external magnetic field is applied in the sample plane, two copper blocks, which can be set to individual temperatures, generate a static out-of-plane temperature gradient, see Fig. 1(a). This thermal perturbation results in a magnonic spin current in the YIG layer[23], thereby transferring angular momentum into the Cu$_{1-x}$Ir$_x$. A spin accumulation builds up, diffuses as a pure spin current and is eventually converted into a transverse charge current by means of the ISHE, yielding a measurable voltage signal. The spin current and consequently the thermal voltage change sign when the YIG magnetization is reversed. The SSE voltage V_{SSE} is defined as the difference between the voltage signals obtained for positive and negative magnetic field divided by 2. Since V_{SSE} is the result of the continuous conversion of a steady spin current, it can, applying the notation of conventional electronics, be considered as a DC signal.

For the ultrafast SSE measurements, the same in-plane magnetized YIG/Cu$_{1-x}$Ir$_x$ samples are illuminated at room temperature by linearly polarized femtosecond laser pulses (energy of 2.5 nJ, duration of 10 fs, center wavelength of 800 nm corresponding to a photon energy of 1.55 eV, repetition rate of 80 MHz) of a Ti:sapphire laser oscillator. Owing to its large bandgap of 2.6 eV[24], YIG is transparent for the incident laser pulse. It is, however, partially (about 50 %) absorbed by the electrons of the Cu$_{1-x}$Ir$_x$ layer, thereby inducing a nonequilibrium electron distribution. In our current understanding[19], the photoexcitation induces additional incoherent spin pumping, that is, the SSE on ultrafast time scales. More precisely, in the course of thermalization, the photogenerated carriers get multiplied, leading to a more frequent scattering of conduction electrons off the metal/insulator interface. As a consequence, an increased random torque is exerted on the YIG magnetic moments, whose rectified component results in an ultrafast transfer of spin angular momentum across the YIG/metal interface[19]. As derived previously[19] using the assumptions of the established SSE model of Ref. 25, the intrinsic time scales of the SSE are so fast that the time (t)-dependent spin-current density, which is polarized along the YIG magnetization, still follows the quasistatic relationship

$$j_{\mathrm{s}}(t) = K \cdot \left[T^{\mathrm{N}}(t) - T^{\mathrm{F}} \right]. \tag{1}$$

Here, K is the SSE coefficient, and $T^{\mathrm{N}}(t)$ denotes the temperature of the conduction electrons in the metallic layer, whose definition can also be extended to the nonequilibrium case[19]. On the other hand, T^{F} describes the magnon temperature in the magnetic insulator[14], which is changed only weakly[19]. In the metal layer, j_{s} is converted into a transverse sub-picosecond charge current through the ISHE, resulting in the emission of a THz electromagnetic pulse into the optical far-field. In our experiment, the THz electric field is sampled using a standard electrooptic detection scheme employing a 1 mm thick ZnTe detection crystal[26]. The magnetic contribution of the THz signal waveform is summarized by calculating the root mean square (RMS) of half the THz signal difference S for positive and negative magnetic fields.

We note that together with our previous THz emission experiments on YIG/Pt and YIG/W layers, we could rule out alternative THz-emission mechanisms: In contrast to semiconductors[27], the pump polarization (linear vs. circular) did not have a measurable impact on the emitted THz waveform, thereby excluding a dominant role of optical orientation in the metal layer. Similarly, the THz signal amplitude was found to follow the YIG magnetization rather than the external magnetic field[19]. Therefore, the Nernst-Ettingshausen effect[28] does not contribute significantly to the THz emission either.

Figures 2(a)-(f) show DC SSE hysteresis loops measured for YIG/Cu$_{1-x}$Ir$_x$/AlOx multilayers with varying Ir concentration x. The temperature difference between sample top and bottom is fixed to $\Delta T = 10\,\mathrm{K}$ with a base temperature of $T = 288.15\,\mathrm{K}$. In the Cu-rich phase, we observe an increase of the thermal voltage signal with increasing x, exhibiting a maximum at $x = 0.3$. Interestingly, upon further increasing the Ir content V_{SSE} reduces again. This behavior is easily visible in Fig. 2(g), in which the SSE coefficient $V_{\mathrm{SSE}}/\Delta T$ is plotted as a function of x. The measured concentration dependence shows that $V_{\mathrm{SSE}}/\Delta T$ exhibits a clear maximum in the range from $x = 0.3$ to 0.5. Thus, as a first key result the maximum spin Hall effect is obtained for the previously neglected alloying regime beyond the dilute doping. For compari-
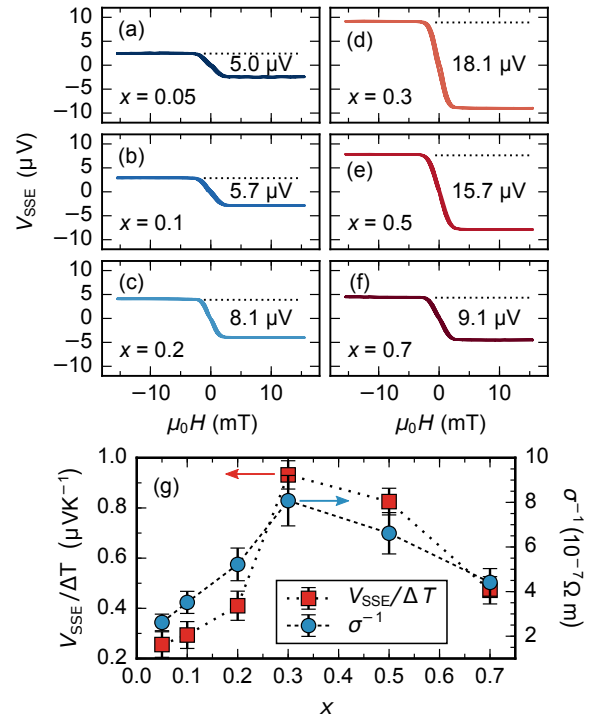

Figure 2: (a)-(f) Measured DC SSE voltage in YIG/Cu$_{1-x}$Ir$_x$/AlOx stacks for different Ir concentrations x in ascending order. The temperature difference between sample top and bottom is fixed to $\Delta T = 10\,\mathrm{K}$. (g) SSE coefficient $V_{\mathrm{SSE}}/\Delta T$ (red squares) and resistivity σ^{-1} (blue circles) as a function of Ir concentration x. While for the former error bars account for the standard error of detected voltage signals and measurement inaccuracies of the temperature difference, the error bars of σ^{-1} include the standard error of the measured film resistances as well as estimated errors of the metal volume determination.

son, the resistivity σ^{-1} of the metal film is also shown in Fig. 2(g). We see that the resistivity of the Cu$_{1-x}$Ir$_x$ layer follows a similar trend as the DC SSE signal.

Typical THz emission signals from the YIG/Cu$_{1-x}$Ir$_x$/AlOx samples are presented in Figs. 3(a)-(f). The THz transients were low-pass filtered in the frequency domain with a Gaussian centered at zero frequency and a full width at half maximum of 20 THz. The RMS of the THz signal that is odd in the sample magnetization is plotted in Fig. 3(g) as a function of x. After an initial signal drop in the Cu-rich phase, the THz signal increases with
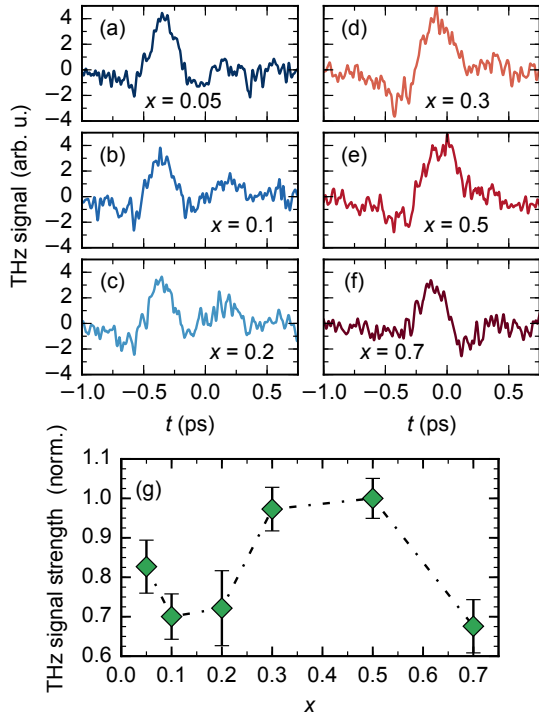
4

Figure 3: (a)-(f) Signal waveforms (odd in the sample magnetization) of the THz pulses emitted from YIG/$Cu_{1-x}Ir_x$/AlOx stacks for different Ir concentrations x in ascending order. (g) THz signal strength (RMS) as a function of Ir concentration x. Error bars take into account the signal-to-noise ratio of the detected signals.

increasing Ir concentration, indicating a signal maximum in the range between $x = 0.3$ and 0.5. Further increase of the Ir content leads to a second reduction of the THz signal strength.

In the following, a direct comparison of the signals obtained from the DC and the ultrafast THz measurements is established. To begin with, the emitted THz electric field right behind the sample is described by a generalized Ohm's law, which in the thin-film limit (film is much thinner than the wavelength and attenuation length of the THz wave within the sample) is in the frequency domain given by[21]

$$\tilde{E}(\omega) \propto \theta_{SH} Z(\omega) \int_0^{d_{CuIr}} dz\, j_s(z,\omega), \quad (2)$$

where ω is the angular frequency. The spin-current density $j_s(z,\omega)$ is integrated over the full thickness d_{CuIr} of the metal film. The total impedance $Z(\omega)$ can be understood as the impedance of an equivalent parallel circuit comprising the metal film ($Cu_{1-x}Ir_x$) and the surrounding substrate (GGG/YIG) and air half-spaces,

$$\frac{1}{Z(\omega)} = \frac{n_1(\omega) + n_2(\omega)}{Z_0} + G(\omega). \quad (3)$$

Here, n_1 and $n_2 \approx 1$ are the refractive indices of substrate and air, respectively, $Z_0 = 377\,\Omega$ is the vacuum impedance, and $G(\omega)$ is the THz sheet conductance of the $Cu_{1-x}Ir_x$ films. Considering the Drude model and a velocity relaxation rate of $28\,THz$ for pure Cu at room temperature as lower boundary[29], the values of $G(\omega)$ vary only slightly over the detected frequency range from 1 to 5 THz (as given by the ZnTe detector crystal). Therefore, the frequency dependence of the conductance can be neglected, i.e. $G(\omega) \approx G(\omega = 0)$. Importantly, the metal-film conductance ($G \approx 8 \times 10^{-3}\,\Omega^{-1}$) is much smaller than the shunt conductance ($[n_1(\omega) + n_2(\omega)]/Z_0 \approx 4 \times 10^{-2}\,\Omega^{-1}$) for the investigated metal film thickness ($d_{CuIr} = 4\,nm$) and can be thus neglected. Therefore, the Ir-concentration influences the THz emission strength only directly through the ISHE-induced in-plane charge current flowing inside the metal layer.

The measured DC SSE voltage, on the other hand, is given by an expression analogous to Eq. (2) and is related to the underlying in-plane charge current by the standard Ohm's law,

$$\frac{V_{SSE}}{\Delta T} \propto \theta_{SH} R \int_0^{d_{CuIr}} dz\, j_s(z). \quad (4)$$

Here, R is the Ohmic resistance of the metal layer between the electrodes, which is inversely proportional to the metal conductivity σ, and $j_s(z)$ is the DC spin current density. Therefore, in contrast to the THz data, the impact of alloying on V_{SSE} through σ^{-1} is significant. For a direct comparison with the THz measurements, we thus contrast the RMS of the THz signal waveform with the DC SSE current density $j_{SSE} = V_{SSE} \cdot \sigma/\Delta T$.

In Fig. 4, the respective amplitudes are plotted as a function of the Ir concentration. Remarkably, DC and THz SSE/ISHE measurements exhibit the very same concentration de-
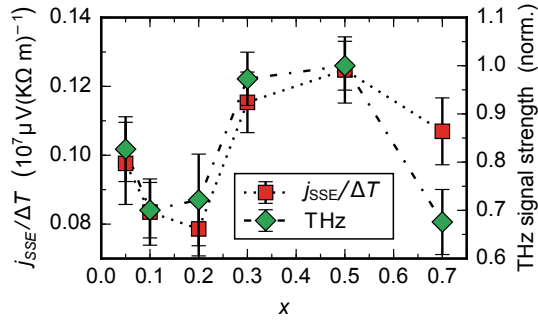
Figure 4: Dependence of the thermal DC spin current (red squares) and the RMS of the THz signal (green diamonds) on the Ir concentration x. The $j_{SSE}/\Delta T$ is calculated by the voltage and resistance data displayed in Fig. 2g, and the error bars are determined by error propagation.

pendence. This agreement suggests that the ISHE retains its functionality from DC up to THz frequencies, which vindicates the interpretation of previous experiments[21]. We emphasize that Fig. 4 also provides further support for our notion that the photoinduced THz emission from YIG/metal bilayers can be considered as an ultrafast version of the SSE. The small discrepancies in Fig. 4 may originate from a variation of the optical absorptance of the near-infrared pump light, which is, however, expected to depend monotonically on x and to only vary by a few percent[21]. Furthermore, as discussed below, these findings imply that for DC and THz spin currents, comparable concentration dependences of spin-relaxation lengths and spin-mixing conductances can be expected. We see for our concrete example good agreement between the DC and THz measurements, and to probe the universality of this consistency, further studies (e.g. using additional systems) are called for.

To discuss the concentration dependence of the DC and THz SSE signals (Fig. 4), we consider Eqs. (2) and (4). According to these relationships, the THz signal and the SSE voltage normalized by the metal resistivity result from a competition of (i) the spin Hall angle θ_{SH} and (ii) the integrated spin-current density $\int_0^{d_{CuIr}} dz \dot{j}_s(z, \omega)$.

To address (i), we consider the local sig-

nal minimum at the small Ir concentration of $x \approx 0.15$ (dilute regime) that appears for both j_{SSE} and the THz amplitude. In fact, one would expect the opposite behavior for θ_{SH} since in the dilute regime the skew scattering mechanism has been predicted[4] and experimentally shown[5] to make the dominant ISHE contribution. Therefore, with increasing density of SOI scattering centers ($\propto \sigma^{-1}$), a linear increase of the spin current signal should appear. This is not observed for j_{SSE} and the THz signal, thereby suggesting that besides θ_{SH} the x-dependence is moreover governed by additional effects. An explanation can be given by (ii), that is the spatial variation of the spin current density which, as discussed below, can be influenced by both electron momentum- and spin-relaxation. The initial electron momenta and spin information of a directional spin current become randomized over length scales characterized by the mean free path ℓ and the spin diffusion length λ_{sd}, yielding a reduction of the spin current density. For spin-relaxation, the integrated spin current density is given by[30]

$$\int_0^{d_{CuIr}} dz j_s(z) \propto \lambda_{sd} \tanh\left(\frac{d_{CuIr}}{2\lambda_{sd}}\right) j_s\left(z = 0^+\right)$$
(5)

with d_{CuIr} being the thickness of the $Cu_{1-x}Ir_x$ layer. According to Niimi *et al.*[5], the spin-diffusion length λ_{sd} decreases exponentially from $\lambda_{sd} \approx 30\,nm$ for $x = 0.01$ to $\lambda_{sd} \approx 5\,nm$ for $x = 0.12$. Despite this exponential decay at small x, the integrated spin current density is nearly constant as long as $\lambda_{sd} > d_{CuIr}$ is true. At large x, λ_{sd} is assumed to saturate and to converge to a finite value, which again yields a constant value for Eq. (5). Solely in the concentration region where $\lambda_{sd} \approx d_{CuIr}$, the integrated spin current density undergoes a significant decline. This effect is capable of explaining the observed reduction of the signal amplitude from $x = 0.05$ to $x = 0.2$. Furthermore, we interpret the fact that for DC and THz SSE signals similar trends are observed as an indication of similar concentration dependences of λ_{sd} in the distinct DC and THz regimes. This notion appears reasonable considering that spin-dependent scattering rates are of the same order

of magnitude as momentum scattering rates[31] (e.g. $1/36\,\mathrm{fs} \approx 28\,\mathrm{THz}$ for Cu[29]) and, thus, above the experimentally covered bandwidth.

Note that the term $j_\mathrm{s}(z = 0^+)$ in Eq. (5) implicitly includes a spin mixing conductance which describes the spin current transparency of the YIG/metal interface via transmission and reflection coefficients. For the DC SSE signals, one needs to consider an effective spin-mixing conductance $g_\mathrm{eff}^{\uparrow\downarrow}$ that incorporates a spin back-flow from CuIr into YIG due to the spin-accumulation build-up at the interface. In the THz measurements, however, the time scale of spin current flow is probably too short to form a sizeable spin accumulation[31]. Considering a potentially concentration-dependent spin-mixing conductance, the matching concentration dependencies observed for DC and THz SSE signals suggest that the spin mixing conductance probed by the THz SSE measurements $g_\mathrm{THz}^{\uparrow\downarrow}$ and the effective spin mixing conductance probed by the DC SSE measurements $g_\mathrm{eff}^{\uparrow\downarrow}$ evolve similarly as a function of x.

In addition to spin-relaxation, the integrated spin current density is influenced by momentum scattering. As shown in Fig. 2, alloying introduces impurities and lattice defects in the dilute phase, such that enhanced momentum scattering rates occur. Assuming that the latter increase more rapidly than θ_SH, the appearance of the previously unexpected local minimum near $x \approx 0.2$ can be thus explained.

We finally focus on the subsequent increase of the spin signal at concentrations $x \geq 0.2$ (concentrated phase). It can be explained by a further increase of extrinsic as well as intrinsic ISHE contributions, as pure Ir itself exhibits a sizeable intrinsic spin Hall effect[2,3]. A quantitative explanation of the intrinsic ISHE, however, requires knowledge of the electron band structure (obtainable by calculations based on the tight-binding model[2] or the density functional theory[32]), which is beyond the scope of this work. The decrease of j_SSE and the THz Signal at $x = 0.7$ may then be ascribed to an increase of atomic order and thus a decrease of the extrinsic ISHE. Given the interplay of the effects that results in the complex concentration dependence, our findings serve as a motivation to further studies beyond the scope of this work that will then determine the contributions more quantitatively.

In conclusion, we compare the spin-to-charge conversion of steady-state and THz spin currents in copper-iridium alloys as a function of the iridium concentration. We find a clear maximum of the spin Hall effect for alloys of around $40\,\%$ Ir concentration, far beyond the previously probed dilute doping regime. While the THz emission signal exhibits a concentration dependence different from the DC spin Seebeck voltage that is often the plotted quantity in DC spin Seebeck measurements, very good qualitative agreement with the DC spin Seebeck current is found. This observation is well understood within our model of THz emission and provides further support of our interpretation that the photoinduced THz emission from YIG/metal bilayers is a signature of the ultrafast version of the spin Seebeck effect. Ultimately, our results show that tuning the spin Hall effect by alloying delivers an unexpected, complex concentration dependence that is equal for spin-to-charge current conversion at DC and THz frequencies. These findings allow us to conclude that the large spin Hall effect in CuIr can be used for spintronic applications on ultrafast time scales.

Acknowledgments

Supporting Information Available

Growth conditions and characterization via X-ray reflectometry of investigated $Cu_{1-x}Ir_x$ thin films.

References

(1) Sinova, J.; Valenzuela, S. O.; Wunderlich, J.; Back, C. H.; Jungwirth, T. *Rev. Mod. Phys.* **2015**, *87*, 1213.

(2) Tanaka, T.; Kontani, H.; Naito, M.; Naito, T.; Hirashima, D. S.; Yamada, K.; Inoue, J. *Phys. Rev. B* **2008**, *77*, 165117.

(3) Morota, M.; Niimi, Y.; Ohnishi, K.; Wei, D. H.; Tanaka, T.; Kontani, H.; Kimura, T.; Otani, Y. *Phys. Rev. B* **2011**, *83*, 174405.

(4) Fert, A.; Levy, P. M. *Phys. Rev. Lett.* **2011**, *106*, 157208.

(5) Niimi, Y.; Morota, M.; Wei, D. H.; Deranlot, C.; Basletic, M.; Hamzic, A.; Fert, A.; Otani, Y. *Phys. Rev. Lett.* **2011**, *106*, 126601.

(6) Niimi, Y.; Kawanishi, Y.; Wei, D. H.; Deranlot, C.; Yang, H. X.; Chshiev, M.; Valet, T.; Fert, A.; Otani, Y. *Phys. Rev. Lett.* **2012**, *109*, 156602.

(7) Zou, L. K.; Wang, S. H.; Zhang, Y.; Sun, J. R.; Cai, J. W.; Kang, S. S. *Phys. Rev. B* **2016**, *93*, 014422.

(8) Ramaswamy, R.; Wang, Y.; Elyasi, M.; Motapothula, M.; Venkatesan, T.; Qiu, X.; Yang, H. *arXiv:1707.09525* **2017**,

(9) Sagasta, E.; Omori, Y.; Isasa, M.; Gradhand, M.; Hueso, L. E.; Niimi, Y.; Otani, Y. C.; Casanova, F. *Phys. Rev. B* **2016**, *94*, 060412(R).

(10) Obstbaum, M.; Decker, M.; Greitner, A. K.; Haertinger, M.; Meier, T. N. G.; Kronseder, M.; Chadova, K.; Wimmer, S.; Ködderitzsch, D.; Ebert, H.; Back, C. H. *Phys. Rev. Lett.* **2016**, *117*, 167204.

(11) Tserkovnyak, Y.; Brataas, A.; Bauer, G. E. W. *Phys. Rev. Lett.* **2002**, *88*, 117601.

(12) Mizukami, S.; Ando, Y.; Miyazaki, T. *Phys. Rev. B* **2002**, *66*, 104413.

(13) Saitoh, E.; Ueda, M.; Miyajima, H.; Tatara, G. *Appl. Phys. Lett.* **2006**, *88*, 182509.

(14) Bauer, G. E. W.; Saitoh, E.; van Wees, B. J. *Nat. Mater.* **2012**, *11*, 391.

(15) Uchida, K.; Adachi, H.; Kikkawa, T.; Kirihara, A.; Ishida, M.; Yorozu, S.; Maekawa, S.; Saitoh, E. *P. IEEE* **2016**, *104*, 1946.

(16) Agrawal, M.; Vasyuchka, V. I.; Serga, A. A.; Kirihara, A.; Pirro, P.; Langner, T.; Jungfleisch, M. B.; Chumak, A. V.; Papaioannou, E. T.; Hillebrands, B. *Phys. Rev. B* **2014**, *89*, 224414.

(17) Schreier, M.; Kramer, F.; Huebl, H.; Geprägs, S.; Gross, R.; Goennenwein, S. T. B.; Noack, T.; Langner, T.; Serga, A. A.; Hillebrands, B.; Vasyuchka, V. I. *Physical Review B* **2016**, *93*, 224430.

(18) Kimling, J.; Choi, G.-M.; Brangham, J. T.; Matalla-Wagner, T.; Huebner, T.; Kuschel, T.; Yang, F.; Cahill, D. G. *Phys. Rev. Lett.* **2017**, *118*, 057201.

(19) Seifert, T. et al. *arXiv:1709.00768* **2017**,

(20) Kampfrath, T.; Battiato, M.; Maldonado, P.; Eilers, G.; Nötzold, J.; Mährlein, S.; Zbarsky, V.; Freimuth, F.; Mokrousov, Y.; Blügel, S.; Wolf, M.; Radu, I.; Oppeneer, P. M.; Münzenberg, M. *Nat. Nanotechnol.* **2013**, *8*, 256–260.

(21) Seifert, T. et al. *Nat. Photonics* **2016**, *10*, 483–488.

(22) Walowski, J.; Münzenberg, M. *J. Appl. Phys.* **2016**, *120*, 140901.

(23) Kehlberger, A.; Ritzmann, U.; Hinzke, D.; Guo, E.-J.; Cramer, J.; Jakob, G.; Onbasli, M. C.; Kim, D. H.; Ross, C. A.; Jungfleisch, M. B.; Hillebrands, B.; Nowak, U.; Kläui, M. *Phys. Rev. Lett.* **2015**, *115*, 096602.

(24) Metselaar, R.; Larsen, P. K. *Solid State Commun.* **1974**, *15*, 291–294.

(25) Adachi, H.; Uchida, K.-i.; Saitoh, E.; Maekawa, S. *Rep. Prog. Phys.* **2013**, *76*, 036501.

(26) Leitenstorfer, A.; Hunsche, S.; Shah, J.; Nuss, M.; Knox, W. *Appl. Phys. Lett.* **1999**, *74*, 1516–1518.

(27) Nastos, F.; Newson, R.; Hübner, J.; van Driel, H.; Sipe, J. *Physical Review B* **2008**, *77*, 195202.

(28) Ettingshausen, A. v.; Nernst, W. *Ann. Phys.* **1886**, *265*, 343–347.

(29) Gall, D. *J. Appl. Phys.* **2016**, *119*, 1–5.

(30) Ando, K.; Takahashi, S.; Ieda, J.; Kajiwara, Y.; Nakayama, H.; Yoshino, T.; Harii, K.; Fujikawa, Y.; Matsuo, M.; Maekawa, S.; Saitoh, E. *J. Appl. Phys.* **2011**, *109*, 103913.

(31) Stern, N. P.; Steuerman, D. W.; Mack, S.; Gossard, A. C.; Awschalom, D. D. *Nat. Phys.* **2008**, *4*, 843.

(32) Guo, G. Y.; Murakami, S.; Chen, T. W.; Nagaosa, N. *Phys. Rev. Lett.* **2008**, *100*, 096401.